Available online at www.sciencedirect.com

ScienceDirect

Advances in Space Research 59 (2017) 1200–1208

ADVANCES IN SPACE RESEARCH (a COSPAR publication)

www.elsevier.com/locate/asr

Dependence of near field co-seismic ionospheric perturbations on surface deformations: A case study based on the April, 25 2015 Gorkha Nepal earthquake

A.S. Sunil [a], Mala S. Bagiya [a,*], Joshi Catherine [b], Lucie Rolland [c], Nitin Sharma [a], P.S. Sunil [a], D.S. Ramesh [a]

[a] *Indian Institute of Geomagnetism (DST), Navi Mumbai 410218, India*
[b] *National Geophysical Research Institute, Uppal Road, Hyderabad 500007, India*
[c] *Université Côte d'Azur, OCA, CNRS, IRD, Géoazur, Sophia-Antipolis, Valbonne, France*

Received 8 October 2016; received in revised form 28 November 2016; accepted 30 November 2016
Available online 10 December 2016

Abstract

Ionospheric response to the recent 25 April 2015 Gorkha, Nepal earthquake is studied in terms of Global Positioning System-Total Electron Content (GPS-TEC) from the viewpoints of source directivity, rupture propagation and associated surface deformations, over and near the fault plane. The azimuthal directivity of co-seismic ionospheric perturbations (CIP) amplitudes from near field exhibit excellent correlation with east-southeast propagation of earthquake rupture and associated surface deformations. In addition, the amplitude of CIP is observed to be very small in the opposite direction of the rupture movement. Conceptual explanations on the poleward directivity of CIP exist in literature, we show the observational evidences of additional equator ward directivity, interpreted in terms of rupture propagation direction. We also discuss the coupling between earthquake induced acoustic waves and local geomagnetic field and its effects on near field CIP amplitudes. We suggest that variability of near field CIP over and near the fault plane are the manifestations of the geomagnetic field-wave coupling in addition to crustal deformations that observed through GPS measurements and corroborated by Interferometric Synthetic Aperture Radar (InSAR) data sets.

Keywords: Co-seismic ionospheric perturbations; Surface deformations; Geomagnetic field-wave coupling

1. Introduction

The seismo-ionospheric coupling is a subject of great fascination. Despite many observations of traveling ionospheric disturbances associated with seismic events, direct phenomenological evidence of this complex coupling has been more difficult to observe. Therefore, the study of any independent seismic event assumes importance, and is viewed as a step forward in gathering observational evidences to understand this coupling mechanism. The earthquake rupture and associated vertical surface deformations and the propagating surface waves (Rayleigh waves) during an earthquake provide a mechanical thrust to the nearby atmosphere, which generates infrasonic acoustic waves in the vicinity of the respective source. In any free running system, once generated, the wave will propagate in all possible directions. The earthquake induced acoustic waves propagate vertically upward with velocity equal to that of the sound (e.g. Heki and Ping, 2005; Astafyeva et al.,

* Corresponding author at: Indian Institute of Geomagnetism, Plot 5, Sector 18, Near Kalamboli Highway, New Panvel (W), Navi Mumbai 410218, India.
E-mail addresses: bagiyamala@gmail.com, mala@iigs.iigm.res.in (M.S. Bagiya).

http://dx.doi.org/10.1016/j.asr.2016.11.041
0273-1177/

2009; Rolland et al., 2011 and references there in). Importantly, these seismically induced acoustic wave disturbances propagate upward in a medium of decreasing atmospheric neutral density. Thus, amplitudes of these disturbances are magnified with altitudes. As these atmospheric neutral waves reach the ionospheric altitudes, the moving neutral particles collide with the ionospheric plasma particles, resulting in electron density disturbances (Kherani et al., 2009). These disturbances could be termed as co-seismic ionospheric perturbations (CIP).

The various characteristics of CIP, like amplitude, phase and directivity/azimuthal asymmetry, depend on several factors such as: (i) magnitude and mechanism of an earthquake (e.g. Astafyeva and Heki, 2009; Astafyeva et al., 2013, 2014; Perevalova et al., 2014; Cahyadi and Heki, 2015) (ii) direction of rupture propagation and allied surface deformations (e.g. Otsuka et al., 2006; Heki et al., 2006; Afraimovich et al., 2010; Kakinami et al., 2012) (iii) alignment of geomagnetic field (e.g. Calais and Minster, 1995; Heki and Ping, 2005; Otsuka et al., 2006; Rolland et al., 2013) (iv) observation geometry (e.g. Heki and Ping, 2005; Rolland et al., 2013) (v) background ionospheric electron density (e.g. Sunil et al., 2015), etc.

In this study, the main emphasis is on the earthquake rupture propagation and its extent besides the azimuthal asymmetry of CIP amplitudes around the epicenter. This is a first study of its kind for the April 2015 Nepal earthquake. Some of the reports on directivity of CIP invoke multiple acoustic sources along the rupture direction as the main hypothesis to explain their observations (Heki et al., 2006), while others explain it in terms of the response of electron density variations to the neutral motion of acoustic waves parallel to the geomagnetic field lines (e.g. Otsuka et al., 2006). In order to investigate these aspects in relation to continental interior (inland) earthquakes, the 25 April 2015 Gorkha (Nepal) earthquake (M_w 7.8) offers a unique opportunity in this context. We attempt to study the behavior of CIP simultaneously just above and near the rupture area (near-field) using available global positioning system (GPS) derived – total electron content (TEC) observations. Unlike other inland earthquakes, the Gorkha event was reasonably well constrained with GPS data available over the rupture area. The observed azimuthal asymmetry of CIP amplitudes around the epicenter is interpreted in terms of rupture propagation direction and also discussed for the effects of coupling between seismically induced acoustic waves and local geomagnetic field around the epicenter. By analyzing ionospheric TEC response to three large earthquakes of different focal mechanisms, Astafyeva and Heki (2009) reported that initial polarity (negative or positive) of CIP depends on the coseismic vertical crustal deformation patterns. Rolland et al. (2013) further suggested that this can be true in regions where geomagnetic field hardly distorts the CIP. In the present case, we corroborate this and suggest that initial polarity of CIP can be directly linked to the crustal deformation patterns only in regions where geomagnetic field seldom disturb the CIP evolution. Therefore, this study is manifold in that context.

2. Surface deformations and TEC observations

The 2015 Mw 7.8 Gorkha earthquake, which occurred on the Main Himalayan Thrust (MHT) depicted in Fig. 1, is the largest earthquake in the region since the 1934 Bihar-Nepal earthquake. The Gorkha event caused considerable damage in Central Nepal including its capital Kathmandu (Sapkota et al., 2012). Inversion of teleseismic data suggests that the main slip occurred due to thrust faulting and is associated with ground acceleration towards east-southeast direction from the epicenter. The rupture propagated for about 160 km with a velocity of 3.1–3.3 km/s resulting in a total source duration of ∼55 s (Fan and Shearer, 2015; Grandin et al., 2015). The deformation map along with surface vertical velocity vectors (Fig. 1) generated respectively from InSAR and GPS observations, suggests an uplift of about 1.0–1.28 m near Kathmandu and a subsidence of about 0.6–0.8 m towards the Northern part of the uplifted area (Lindsey et al., 2015; Sreejith et al., 2016). However, joint inversion of this GPS and InSAR data suggest a thrust slip with a coseismic component of about 5.7 m at 12 km depth.

GPS derived TEC is a characteristic observable to monitor the ionospheric variations (e.g. Rama Rao et al., 2006; Bagiya et al., 2009 and references there in). It can be defined as a line integral of electron density along the satellite-receiver radio line of sight. The unit of TEC is TECU, which is 10^{16} electrons per square meter, i.e. the total number of free electrons in a column with cross sectional area of 1 m^2. TEC variations from available GPS stations (responsible agencies are listed in Table 1) are derived using differential carrier phase and code measurements available in the receiver independent exchange (RINEX) format at every 30 s. The slant TEC (sTEC) is estimated from code measurements and smoothed with the carrier phase measurements. The resultant smoothed TEC values are not absolute but contain satellite and receiver hardware biases. In the present study, we mostly concentrate on TEC changes and thus the estimation of absolute TEC may not be required. We prefer to show the CIP variability using sTEC in order to minimize the ambiguity in identifying the initial phase of TEC variations that may arise during detrending process.

3. Near field CIP response

Using GPS occultation technique, Sun et al. (2016) studied the ionospheric F2 region perturbations associated with same Nepal earthquake and reported that the earthquake induced ground deformations can significantly perturb the vertical ionospheric electron density structure. It is documented that CIP within the area of ∼800 km surrounding an earthquake epicenter are mainly caused by the acoustic waves direct from the epicenter (e.g. Otsuka et al., 2006). In

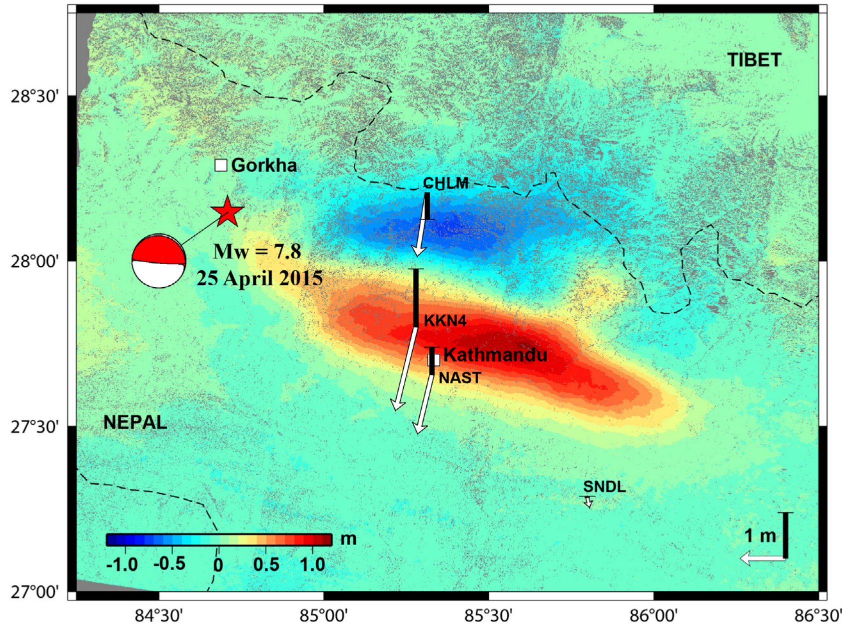

Fig. 1. Map illustrates the co-seismic horizontal and vertical vectors and deformation image generated from GPS and InSAR data respectively (after Lindsey et al., 2015; Sreejith et al., 2016). White and black arrows represent GPS horizontal and vertical vectors respectively. Negative and Positive values in color bar indicate the ground subsidence and uplift due to Gorkha earthquake respectively. The location of earthquake epicenter is shown as red star. (For interpretation of the references to color in this figure legend, the reader is referred to the web version of this article.)

Table 1
GPS stations along with responsible agency/group.

Station code	Geographic latitude	Geographic longitude	Responsible agency/group
brn2	26.52	87.27	NEGAR Nepal
bhgp	25.23	87.05	ISM Dhanbad
bika	28.03	73.26	University of Udaipur
chlm	28.21	85.31	NEGAR Nepal
dngd	28.75	80.59	NEGAR Nepal
dnsg	28.34	83.76	NEGAR Nepal
grhi	27.95	82.49	NEGAR Nepal
jmsm	28.81	83.74	NEGAR Nepal
lck3	26.91	80.96	IGS
lhaz	29.66	91.1	IGS
nani	29.38	79.45	NGRI Hyderabad
nast	27.66	85.33	NEGAR Nepal
ptna	25.59	85.14	ISM Dhanbad

reference to this, the CIP within 800 km surrounding the epicenter are considered as near field CIP in the present study. The various characteristics of the near field CIP after April 2015 Gorkha earthquake are demonstrated in Figs. 2–4. Fig. 2(a) shows the various station locations and trajectory of ionospheric piercing points (IPP) at 350 km for PRN 16 from the respective station. The blue disk represents the CIP with initial TEC response as TEC depletion, while the CIP with initial TEC response as TEC enhancement are shown in red color. The near field CIP variability with time as observed by PRN 16 in sTEC is shown in Fig. 2(b). CIP variability, in Fig. 2, around the epicenter suggests that amplitudes of CIP are clearly and preferentially larger east-southeast (region 2 and 4 in Fig. 2). In region 2, chlm_PRN16 observed maximum sTEC perturbation of ~0.7 TECU with TEC depletion as initial phase while in region 4 ptna_PRN16 recorded maximum sTEC perturbation of ~2.91 TECU with TEC enhancement as initial phase. In region 3, sTEC perturbation observed as initial TEC enhancement of ~0.72 TECU by alh2_PRN16. CIP amplitudes, as observed by PRN 16, towards the west (region 1 in Fig. 2(a) and (b)) are rather feeble. The first onset of CIP is seen at chlm_PRN 16, in the east, after ~9 min of the earthquake occurrence. To the west, the first CIP onset is detected at dnsg_PRN 16~11 min after the event. The observed time delay of ~9–11 min confirms the acoustic wave as a source of the near field CIP. PRN 16 observations suggest that significant CIP amplitudes occurred in the east-southeast of the epicenter.

Fig. 3(a) depicts the station locations and trajectory of IPP at 350 km for PRN 23. The near field CIP variability with time as observed by PRN 23 is shown in Fig. 3(b). CIP variability in region 1 is again feeble as observed by PRN 23 and it is significant in region 2 (brn2_PRN23, ~1.99 TECU, TEC depletion as initial phase) and 4 (bhgp_PRN23, ~1.2 TECU, TEC enhancement as initial phase). This corroborates the azimuthal asymmetry of near field CIP amplitudes as observed by PRN 16.

The IPP tracks for PRN 26, 03 and 27 at ~350 km and the observable stations are shown in Fig. 4(a). It could be observed in Fig. 4(b) that outside the region of 250 km radius (inner circle in Fig. 4(a)), the CIP amplitudes started decreasing in region 2. In region 3, alh2_PRN26 observed

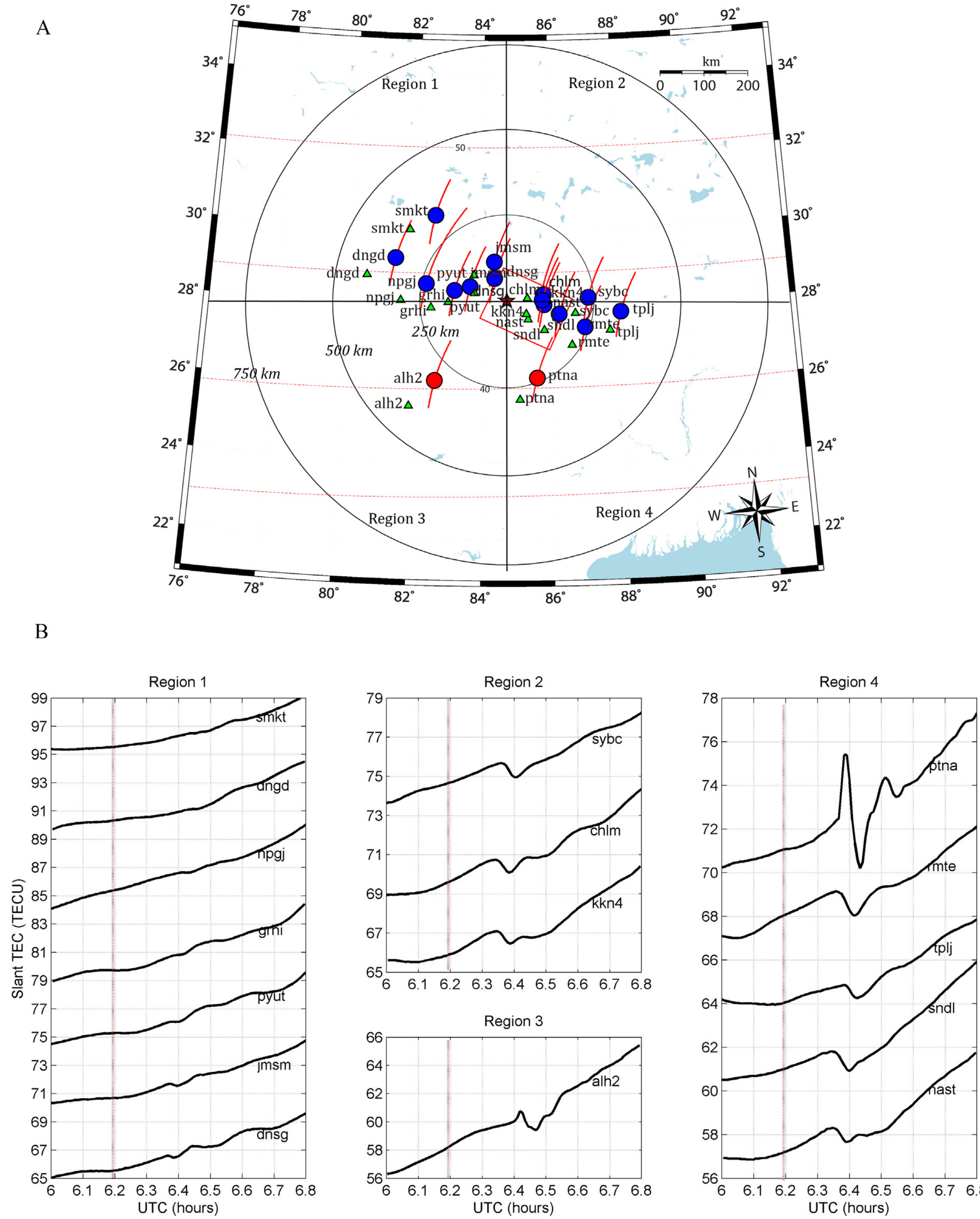

Fig. 2. Evolution of near field CIP surrounding the epicenter within radius of ~ 800 km as observed by PRN 16. (a) Four regions are identified for easy explanation. The disk location shows the position of IPP at detection time of CIP. Blue disk shows depletion as initial TEC response while red disk shows enhancement as initial TEC response. Each disk is labeled with the station code from where it has been observed. Geographical location of each station is shown by green triangle. The fault plane area is shown by red rectangle. The horizontal dashed red lines present the magnetic inclination at that location. (b) temporal variations of sTEC over the four regions. CIP in terms of TEC depletions are observed right over and nearby the fault plane area, mainly in the north of the epicenter while enhancements observed in the south. (For interpretation of the references to color in this figure legend, the reader is referred to the web version of this article.)

TEC enhancement of ~0.75 TECU and in region 4 ptna_PRN26 recorded enhancement of ~0.49 TECU. In Fig. 4(c), significant TEC enhancements recorded by PRN 3. In region 4, maximum TEC enhancement of

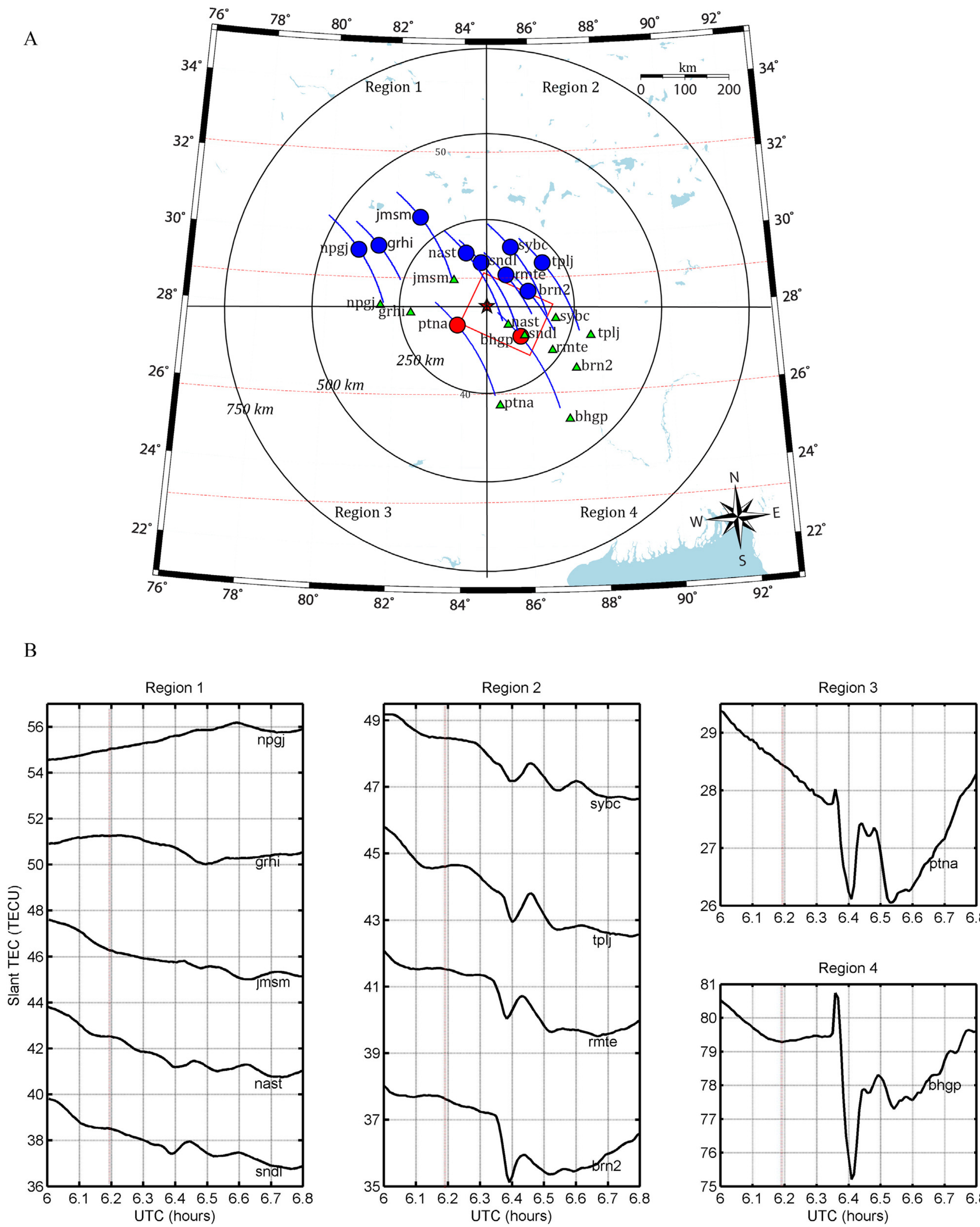

Fig. 3. Near field CIP characteristics as observed by PRN 23. (a) Various station locations and IPP tracks for PRN 23 from the respective station. The blue disk represents the CIP with initial TEC response as TEC depletion, while the CIP with initial TEC response as TEC enhancement are shown in red color. (b) Near field CIP variability with time as observed by PRN 23. Significant CIP recorded by PRN 26 in south-southeast of the epicenter with TEC enhancement as initial phase. (For interpretation of the references to color in this figure legend, the reader is referred to the web version of this article.)

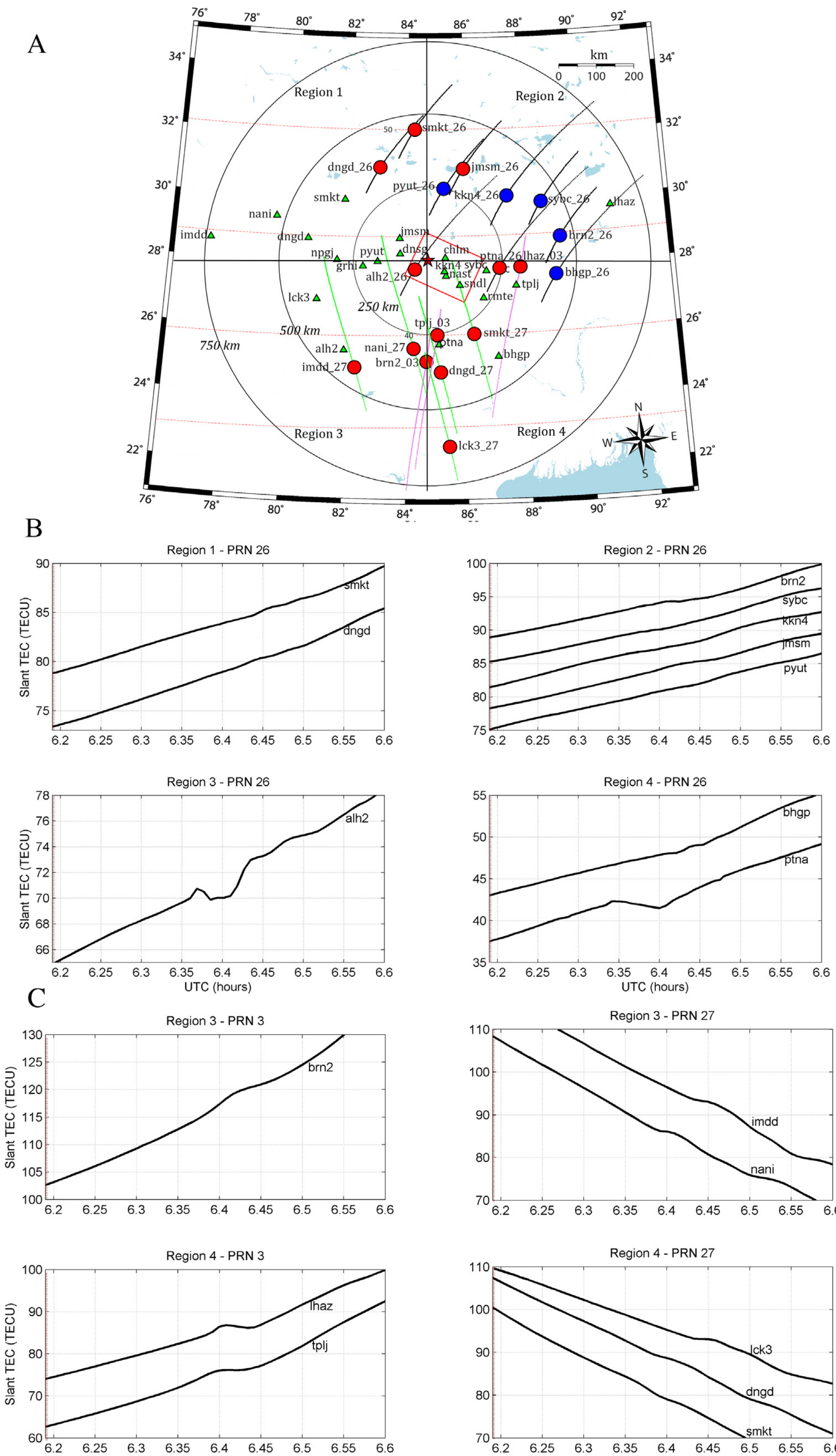

Fig. 4. Near field CIP characteristics as observed by PRN 26, 03 and 27. (a) Same as Fig. 2(a) and 3(a) but for PRN 26, 03 and 27. (b) CIP variability as observed by PRN 26 around the epicenter (c) same as (b) but for PRN 03 and 27.

~1.62 TECU observed by lhaz_PRN3 while in region 3 the maximum TEC enhancement of ~2.5 TECU observed by brn2_PRN3.

4. Discussion

Earthquakes of moderate magnitude and dominant uplift can be approximated with a point source, emitting waves of equivalent amplitudes isotropically (Rolland et al., 2013). Seismic waves after a large earthquake show larger amplitudes in the direction of rupture (Courboulex et al., 2013). The observed surface deformations from GPS and InSAR depicted in Fig. 1 demonstrate that the rupture extended in the east-southeast direction (Lindsey et al., 2015; Sreejith et al., 2016). The azimuthal directivity of near field CIP observed in the present case shows good correlation with east-southeastward rupture propagation. Using model calculations, Otsuka et al. (2006) have discussed the directivity of CIP during 2004 great Sumatra earthquake in terms of the response of electron density variations to the neutral motion of acoustic waves in oblique geomagnetic field lines. Following this, Heki et al. (2006) have explained the directivity assuming linearly distributed multiple acoustic wave sources over the fault segments from Sumatra to Andaman Island. Right over the epicenter, the seismic rupture cannot be assimilated to a point source, but at far field it can be considered as a point source. During the Sumatra 2004 great earthquake, the rupture propagated to a distance of ~1300 km within ~8 min i.e. higher than the characteristic period of ~4 to 5 min for acoustic waves in upper atmosphere. Thus, it was feasible to visualize multiple sources even at far field. In the present case study, the rupture propagated only up to ~160 km in the east-southeast direction within 55 s (Fan and Shearer, 2015; Grandin et al., 2015). Here, as the rupture duration (55 s) is lower than the characteristic period of acoustic waves (~4 to 5 min) in upper atmosphere, it could be treated as an extended and continuous source. Thus, we suggest that the observed azimuthal directivity of near field CIP prefer to follow the extended and continuous rupture that propagated in the east-southeast direction. The existence of acoustic waves as the source for the near field CIP could be confirmed with the velocity estimation shown in Fig. 5. The near field CIP, within radius of 800 km, at south of the epicenter are considered for velocity estimation and the estimated velocity is of 1.022 km/s.

In order to verify the effect of geomagnetic field over the observed azimuthal asymmetry of CIP amplitudes around the epicenter, the factor representing the coupling between acoustic wave vector and local geomagnetic field at ionospheric height of ~350 km are derived and presented in Fig. 6. This coupling factor is same as that reported by Rolland et al. (2013). The location of epicenter and a circle with radius of ~250 km are also shown in Fig. 6. The coupling factor, higher south of the epicenter supports the equatorward propagation and amplification of CIP in southern part. The same is observed to hamper the propagation of CIP in north of the epicenter. Though the coupling factor is supportive, both, in southwest and southeast of the epicenter, the significant CIP amplitudes observed mainly in the east-southeast. We suggest here that the significant CIP in east-southeast of the epicenter are the combined effect of tectonic forcing and geomagnetic field-acoustic wave coupling. As the prime tectonic energy propagated in the east-southeast direction, the CIP manifestations in the same direction are prominent. In north of the epicenter, the effects of geomagnetic field-acoustic wave coupling observed as reduction in CIP amplitudes with distance. It could be noticed that although the geometry of the observable satellites are different, near field CIP distribution around the epicenter as observed by these satellites prefer to follow the rupture induced seismic energy distribution and geomagnetic field- acoustic wave coupling.

It could be seen (Figs. 2–4) that CIP over the fault plane area, particularly in northeast and northwest of the epicenter are mostly associated with TEC depletions (regions 1 and 2), while the east and southeast locations record mostly enhanced TEC (regions 3 and 4). Astafyeva and Heki (2009) reported the variations in phases of the seismic induced waveforms at ionospheric heights caused by coseismic crustal deformation patterns. They suggested that the coseismic crustal subsidence generates acoustic waves with rarefaction as the initial phase polarity, which they named as inverted N-type perturbations, while the uplift generates acoustic waves lead by compression as the initial phase. The inverted N-type waveforms manifest as depletion in TEC following the earthquake. At the same

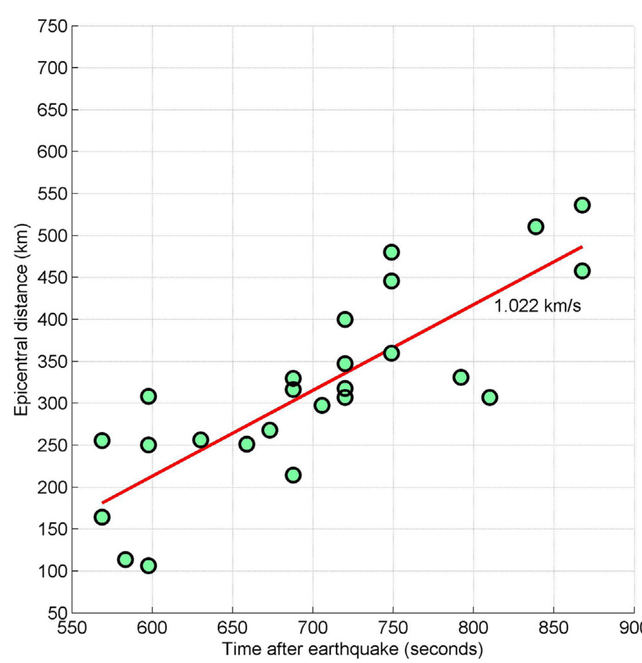

Fig. 5. Velocity estimation for near field CIP using epicentral distance and the onset time of CIP. The slope exhibits that near field CIP travel with acoustic velocity.

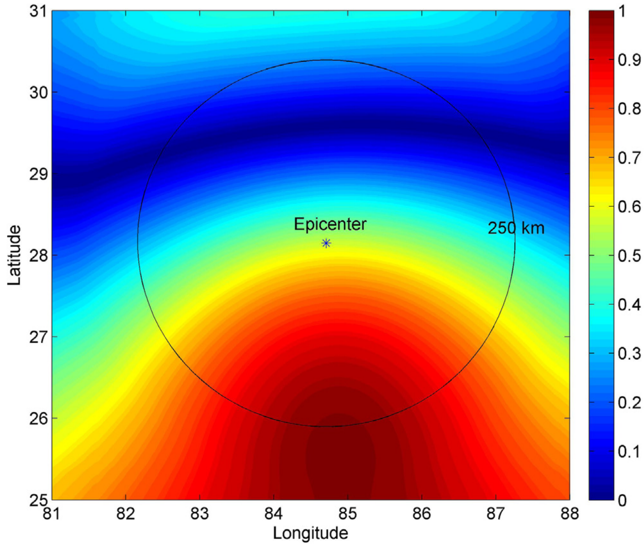

Fig. 6. Coupling between seismic induced acoustic waves and local geomagnetic field at the epicenter. The coupling factor is derived at the height of ~350 km.

time, the regular N-type waveforms are seen as enhancement in TEC as initial response. Though, the generation and propagation of inverted N-type wave up to ionospheric heights is not very simple due to its lower velocity than the following compression phase (Astafyeva and Heki, 2009). Rolland et al. (2013) reported that initial polarity of CIP mainly controlled by geomagnetic field and thus the effects of coseismic crustal deformation patterns on the polarity of very first ionospheric perturbations are more prominent in the regions where geomagnetic field seldom deforms the CIP. Following this, we suggest here that the negative polarity of CIP over the subsidence regions (blue disks in Figs. 2–4) cannot be directly linked to the land subsidence as the geomagnetic field (Fig. 6) is observed to hamper the propagation of CIP in the north.

Kamogawa et al. (2015) have reported TEC depletions around the epicenter for the same Nepal earthquake. They proposed that not only tsunami (Kakinami et al., 2012) but shallow inland earthquakes with magnitude more than 7 can also generate TEC depletions or the so called ionospheric hole. It should however be noted that we obtained similar results for this Gorkha inland earthquake based on a refined analysis of the space-time characteristics of near-field perturbations using larger number of observations. We propose here that the observed TEC depletion in north of the epicenter is mainly the effects of geomagnetic field-wave coupling.

5. Conclusion

The azimuthal asymmetry in the spatial variations of near field CIP related to the Nepal earthquake of April 25, 2015 is studied for the first time. We suggest that the azimuthal asymmetry of near field CIP prefer to follow the east-southeast propagated rupture. We propose here that due to the small length, ~160 km, the rupture acted as an extended and continuous source for acoustic waves. The significant CIP in the east-southeast direction are the combined effect of tectonic forcing and favorable geomagnetic field-acoustic wave coupling. The geomagnetic field-acoustic wave coupling observed to hamper the CIP propagation in north of the epicenter. We also suggest that initial polarity of CIP over the subsidence regions could not be directly linked to the crustal deformation patterns as the geomagnetic field observed to distort the CIP in the north. The present detailed study could be appreciated in elucidating more on the effects of seismic rupture extent and propagation direction on the ionosphere.

Acknowledgements

The authors gratefully acknowledge the UNAVCO (https://www.unavco.org/data/) for providing GPS data. InSAR data is available at http://topex.ucsd.edu/nepal/. The authors are grateful to several individuals from various organizations for the GPS ionospheric data at Indian locations of bhgp, bika, nani, and ptna. In this regard, P. N. S. Roy, P. K. Khan, Javed Malik, Harsh Bhu and N. Puviarasan and their respective organizations are gratefully acknowledged. This data is available with JC. This work is part of the new inter disciplinary initiative, Litho sphere-Atmosphere-Ionosphere-Magnetosphere (LAIM) coupling, of Indian Institute of Geomagnetism (IIG), Navi Mumbai, India. This work is supported by Department of Science and Technology (), India. AS is grateful to the DST, India for providing the research fellowship.

References

Afraimovich, E.L., Feng, D., Kiryushkin, V.V., Astafyeva, E.I., 2010. Near-field TEC response to the main shock of the 2008 Wenchuan earthquake. Earth Planets Space 62, 899–904.

Astafyeva, E., Heki, K., 2009. Dependence of waveform of near-field coseismic ionospheric disturbances on focal mechanisms. Earth Planets Space 16, 939–943.

Astafyeva, E., Heki, K., Kiryushkin, V., Afraimovich, E.L., Shalimov, S., 2009. Two-mode long- distance propagation of coseismic ionosphere disturbances. J. Geophys. Res. 114, A10307. http://dx.doi.org/10.1029/2008JA013853.

Astafyeva, E., Shalimov, S., Olshanskaya, E., Lognonné, P., 2013. Ionospheric response to earthquakes of different magnitudes: larger quakes perturb the ionosphere stronger and longer. Geophys. Res. Lett. 40, 1675–1681. http://dx.doi.org/10.1002/grl.50398.

Astafyeva, E., Rolland, L.M., Sladen, A., 2014. Strike-slip earthquakes can also be detected in the ionosphere. Earth. Planet. Sci. Lett. 405, 180–193.

Bagiya, M.S., Joshi, H.P., Iyer, K.N., Aggarwal, M., Ravindran, S., Pathan, B.M., 2009. TEC variations during low solar activity period (2005–2007) near the Equatorial Ionospheric Anomaly Crest region in India. Ann. Geophys. 27, 1047–1057.

Calais, E., Minster, J.B., 1995. GPS detection of ionospheric perturbations following the January 17, 1994, Northridge earthquake. Geophys. Res. Lett. 22, 1045–1048. http://dx.doi.org/10.1029/95GL00168.

Cahyadi, M.N., Heki, K., 2015. Coseismic ionospheric disturbance of the large strike-slip earthquakes in North Sumatra in 2012: Mw dependence of the disturbance amplitudes. Geophys. J. Int. 200 (1), 116–129. http://dx.doi.org/10.1093/gji/ggu343.

Courboulex, F., Dujardin, A., Vallée, M., Delouis, B., Sira, Ch., Deschamps, A., Honoré, L., Thouvenot, F., 2013. High-frequency directivity effect for an M_w 4.1 earthquake, widely felt by the population in southeastern France. Bull. Seism. Soc. Am. 103 (6), 3347–3353.

Fan, W., Shearer, P.M., 2015. Detailed rupture imaging of the 25 April 2015 Nepal earthquake using teleseismic *P* waves. Geophys. Res. Lett. 42, 5744–5752. http://dx.doi.org/10.1002/2015GL064587.

Grandin, R., Vallee, M., Satriano, C., Lacassin, R., Klinger, Y., Simoes, M., Bollinger, L., 2015. Rupture process of the *Mw*=7.9 2015 Gorkha earthquake (Nepal): insights into Himalayan megathrust segmentation. Geophys. Res. Lett. 42, 8373–8382. http://dx.doi.org/10.1002/2015GL066044.

Heki, K., Ping, J., 2005. Directivity and apparent velocity of the coseismic ionospheric disturbances observed with a dense GPS array. Earth Planet Sci. Lett. 236, 845–855. http://dx.doi.org/10.1016/j.epsl.2005.06.010.

Heki, K., Otsuka, Y., Choosakul, N., Hemmakorn, N., Komolmis, T., Maruyama, T., 2006. Detection of ruptures of Andaman fault segments in the 2004 Great Sumatra Earthquake with coseismic ionospheric disturbances. J. Geophys. Res. 111, B09313. http://dx.doi.org/10.1029/2005JB004202.

Kakinami, Y., Kamogawa, M., Tanioka, Y., Watanabe, S., Gusman, A. R., Liu, J.Y., Watanabe, Y., Mogi, T., 2012. Tsunamigenic ionospheric hole. Geophys. Res. Lett. 39, L00G27. http://dx.doi.org/10.1029/2011GL050159.

Kamogawa, M., Kanaya, T., Orihara, Y., Toyoda, A., Suzuki, Y., Togo, S., Liu, J.Y., 2015. Does an ionospheric hole appear after an inland earthquake? J. Geophys. Res. http://dx.doi.org/10.1002/2015JA021476.

Kherani, E.A., Lognonné, P., Kamath, N., Crespon, F., Garcia, R., 2009. Response of the ionosphere to the seismic triggered acoustic waves: electron density and electromagnetic fluctuations. Geophys. J. Int. 176, 1–13. http://dx.doi.org/10.1111/j.1365-246X.2008.03818.x.

Lindsey, E., Natsuaki, R., Xu, X., Shimada, M., Hashimoto, H., Melgar, D., Sandwell, D., 2015. Line of sight deformation from ALOS-2 interferometry: *Mw* 7.8 Gorkha earthquake and *Mw* 7.3 aftershock. Geophys. Res. Lett. 42, 6655–6661. http://dx.doi.org/10.1002/2015GL065385.

Otsuka, Y., Kotake, N., Tsugawa, T., Shiokawa, K., Ogawa, T., Effendy Saito, S., Kawamura, M., Maruyama, T., Hemmakorn, N., Komolmis, T., 2006. GPS detection of total electron content variations over Indonesia and Thailand following the 26 December 2004 earthquake. Earth Planets Space 58, 159–165.

Perevalova, N.P., Sankov, V.A., Astafyeva, E., Zhupityaeva, A.S., 2014. Threshold magnitude for ionospheric TEC response to earthquakes. J. Atmos. Solar-Terr. Phys. 108, 77–90.

Rama Rao, P.V.S., Gopi Krishna, S., Niranjan, K., Prasad, D.S.V.V.D., 2006. Temporal and spatial variations in TEC using simultaneous measurements from the Indian GPS network of receivers during the low solar activity period of 2004–2005. Ann. Geophys. 24, 3279–3292.

Rolland, L.M., Lognonné, P., Astafyeva, E., Kherani, A., Kobayashi, N., Mann, M., Munekane, H., 2011. The resonant response of the ionosphere imaged after the 2011 Tohoku-Oki earthquake. Earth Planet Space 63, 853–857. http://dx.doi.org/10.5047/eps.2011.06.020.

Rolland, L.M., Vergnolle, M., Nocquet, J.M., Sladen, A., Dessa, J.X., Tavakoli, F., Nankali, H.R., Cappa, F., 2013. Discriminating the tectonic and non-tectonic contributions in the ionospheric signature of the 2011, Mw 7.1, dip-slip Van earthquake, Eastern Turkey. Geophys. Res. Lett. 40 (11), 2518–2522. http://dx.doi.org/10.1002/grl.50544.

Sapkota, S.N., Bollinger, L., Klinger, Y., Tapponnier, P., Gaudemer, Y., Tiwari, D., 2012. Primary surface ruptures of the great Himalayan earthquakes in 1934 and 1255. Nat. Geosci. 6, 71–76. http://dx.doi.org/10.1038/ngeo1669.

Sun, Y.-Y., Liu, J.Y., Lin, C.Y., Tsai, H.F., Chang, L.C., Chen, C.Y., Chen, C.H., 2016. Ionospheric F2 region perturbed by the 25 April 2015 Nepal earthquake. J. Geophys. Res. Space Phys. 121, 5778–5784. http://dx.doi.org/10.1002/2015JA022280.

Sunil, A.S., Bagiya, M.S., Reddy, C.D., Kumar, M., Ramesh, D.S., 2015. Post-seismic ionospheric response to the 11 April 2012 east Indian Ocean doublet earthquake. Earth Planets Space. http://dx.doi.org/10.1186/s40623-015-0200-8.

Sreejith, K.M., Sunil, P.S., Agrawal, R., Saji, A.P., Ramesh, D.S., Rajawat, A.S., 2016. Coseismic and early postseismic deformation due to the 25 April 2015, M_w 7.8 Gorkha, Nepal earthquake from InSAR and GPS measurements. Geophys. Res. Lett. http://dx.doi.org/10.1002/2016GL067907.